Journal of Atmospheric and Solar-Terrestrial Physics 162 (2017) 97–105

Contents lists available at ScienceDirect

Journal of Atmospheric and Solar-Terrestrial Physics

journal homepage: www.elsevier.com/locate/jastp

Large ice particles associated with small ice water content observed by AIM CIPS imagery of polar mesospheric clouds: Evidence for microphysical coupling with small-scale dynamics

D. Rusch [a,*], G. Thomas [a], A. Merkel [a], J. Olivero [c], A. Chandran [a], J. Lumpe [b], J. Carstans [d], C. Randall [a], S. Bailey [d], J. Russell III [e]

[a] Laboratory for Atmospheric and Space Physics, University of Colorado, Boulder, CO, United States
[b] Computational Physics, Inc., Boulder, CO, United States
[c] Center for Space & Atmospheric Research, Embry-Riddle Aeronautical University, Daytona Beach, FL, United States
[d] Bradley Department of Electrical and Computer Engineering, Virginia Tech, Blacksburg, VA, United States
[e] Center for Atmospheric Sciences, Hampton University, Hampton, VA, United States

ARTICLE INFO

Article history:
Received 11 January 2016
Received in revised form
29 April 2016
Accepted 30 April 2016
Available online 2 May 2016

Keywords:
Polar mesospheric clouds
Mesosphere dynamics
Gravity waves

ABSTRACT

Observations by the Cloud Imaging and Particle Size (CIPS) instrument on the Aeronomy of Ice in the Mesosphere (AIM) satellite have demonstrated the existence of Polar Mesospheric Cloud (PMC) regions populated by particles whose mean sizes range between 60 and 100 nm (radii of equivalent volume spheres). It is known from numerous satellite experiments that typical mean PMC particle sizes are of the order of 40–50 nm. Determination of particle size by CIPS is accomplished by measuring the scattering of solar radiation at various scattering angles at a spatial resolution of 25 km^2. In this size range we find a robust anti-correlation between mean particle size and albedo. These very-large particle-low-ice (VLP-LI) clouds occur over spatially coherent areas. The surprising result is that VLP-LI are frequently present either in the troughs of gravity wave-like features or at the edges of PMC voids. We postulate that an association with gravity waves exists in the low-temperature summertime mesopause region, and illustrate the mechanism by a gravity wave simulation through use of the 2D Community Aerosol and Radiation Model for Atmospheres (CARMA). The model results are consistent with a VLP-LI population in the cold troughs of monochromatic gravity waves. In addition, we find such events in Whole Earth Community Climate Model/CARMA simulations, suggesting the possible importance of sporadic downward winds in heating the upper cloud regions. This newly-discovered association enhances our understanding of the interaction of ice microphysics with dynamical processes in the upper mesosphere.

1. Introduction

Polar Mesospheric Clouds (PMCs) have been a subject of study for many years using ground based, rocket, and satellite observations. PMCs (or their ground-based manifestations, noctilucent clouds, NLC) are also sensitive indicators of gravity waves (GW) and instability dynamics (Witt, 1962; Fritts et al., 1993). They have an advantage over airglow measurements in defining GW properties in that they occur in thin (1–2 km) layers and thus do not smear out vertical structure. They also provide sensitive indicators of changes of temperature (Merkel et al., 2008; Hervig et al., 2015 and references therein). The Aeronomy of Ice in the Mesosphere (AIM) mission (Russell et al., 2009) is designed to provide unique information on PMCs, to reveal their temporal variations, and enhance the basic understanding of the physics involved in their production and destruction. Here we report on measurements of clouds having very large mean ice particle sizes. We call these for short, Very-Large-Particle-Low-Ice events (VLP-LI) having mode radii greater than 60 nm, and associated with regions of comparatively low values of cloud albedo. The column-integrated ice water content (IWC) is roughly proportional to UV albedo (e.g. DeLand and Thomas, 2015). The VLP-LI clouds have values typically less than 50 /km^2, compared with'normal' values of 100 g/km^2 and extremes up to 200 g/km^2 or more.

Ice-particle shapes have long been expected to be non-spherical, but only recently has their shape been shown to be optically equivalent to oblate spheroids with small axial ratios (Baumgarten et al., 2002; Rapp et al., 2007; Hervig et al., 2009). It is conventional to define mean particle size in terms of the radius of the sphere with the same mass. We should also note that if the

* Corresponding author.
E-mail address: dave.rusch@lasp.colorado.edu (D. Rusch).

http://dx.doi.org/10.1016/j.jastp.2016.04.018
1364-6826/

particle size distribution is Gaussian, as often assumed in the literature (Berger and von Zahn, 2002; Rapp and Thomas, 2006), the mode radius (r_m) and the mean radius are identical, at least for the size range observable by CIPS. We thus use these terms interchangeably, and will often simply refer to this quantity as 'size'.

The 'standard' model of Polar Mesospheric Clouds specifies that nucleation is centered in the uppermost region of the cloud layer, near the mesopause, and that the ice particles grow as they descend and tend to be larger at lower levels approaching the cloud base. Observing the different ice particle populations is challenging mostly because most remote sensing methods involve spatial averaging through many cloud structures of disparate brightnesses. Lidar studies are an exception to this averaging case.

The occurrence of mean particle sizes greater than 60 nm in remote-sensing retrievals is not new. For a review of observations, see Baumgarten et al. (2008). This population has been recently highlighted in height-resolving tomographic retrievals of UV satellite data taken by the Optical Spectrograph and Infrared Imager System (OSIRIS) experiment (Hultgren et al., 2013; Hultgren and Gumbel, 2014). These authors showed that the largest particles reside at the normal cloud base, near 80 km, and range in size up to 120 nm. They also found that the number density of these particles is so small that the more numerous ice particles of smaller sizes (30–50 nm) lying above (typically from 82–84 km) contribute the 'lion's share' of the scattered radiance. In their words "*a nadir-viewing technique can only "see" the larger particles when observing cloud areas where no bright cloud layers are situated above the larger particles*." In this paper, we show that with the superior spatial resolution and large areal coverage of CIPS, such conditions are surprisingly frequent, and moreover, when they occur they are almost always associated with dynamically-driven structures, caused possibly by gravity waves.

In Section 2, we describe the CIPS data and its ability to measure mean cloud particle size. Section 3 describes the results derived from a phase function analysis of the angular scattering information. Section 4 contains a comparison with other PMC experiments. Section 5 provides a discussion and simulations of VLP-LI from two microphysical models. Section 6 contains a summary and conclusions.

2. Data

The Cloud Imaging and Particle Size (CIPS) instrument on AIM (McClintock et al., 2009) consists of four nadir-pointing cameras that image the atmosphere's scattered UV brightness (albedo) with a band pass centered at 265 nm and extending from 258 nm to 274 nm (half-power points). The four cameras have an overlapping field of view of 120° (along orbit track) and 80° (cross orbit track). The details of the instrumentation, camera configuration and first results can be found in Rusch et al. (2009) and McClintock et al. (2009). Orbit 'strips' are made by merging together the individual camera images taken each orbit. CIPS cameras take an image every 43 s with an exposure time of 1 s. On average, each camera takes 26 images per orbit over the sunlit summer polar region. A description of the various CIPS data products is available online at the AIM site, http://aim.hamptonu.edu/library/documentation/instruments/cips/cips_docs.html. The data processing algorithms are described in Lumpe et al. (2013).

The CIPS observational technique provides measurements of PMC scattering at several scattering angles through spatially-coincident measurements of the same scattering volume. In Fig. 1 we show, for various assumptions of particle size distributions and particle shapes, the ratio of forward (45°) to backward (135°) scattering as a function of mean particle radius (this ratio is hereafter referred to as FBR). We emphasize that CIPS measures

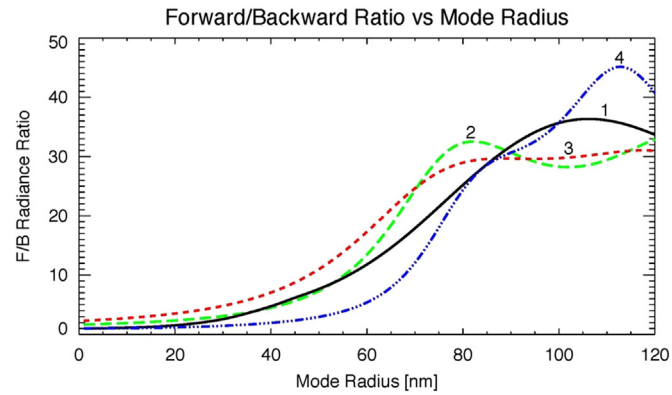

Fig. 1. Forward (scattering angle = 45°)/Backward (scattering angle = 135°) ratios of theoretical scattering coefficients (or radiances) vs. mode particle radius. Calculated from T-matrix code, assuming oblate spheroidal shapes with different axial ratios (AR) and different Gaussian distribution widths, s. (1) Solid dark curve: Gaussian (AR = 2) with variable s, increasing linearly with mode radius r_m from 1 nm to 16 nm at r_m = 40 nm and remaining at s = 16 nm for r_m > 40 nm (the size distribution used by CIPS); (2) green curve with long dashes: AR = 1 (spherical particles) with a constant Gaussian width of 12 nm for all r_m; (3) red curve with short dashes: Gaussian with spherical particles (AR = 1) with s = 20 nm; (4) blue curve with long dash and three short dashes: monodisperse case (AR = 2), where the mode radius is simply the cloud particle radius. All sizes are expressed in terms of the radius of a sphere of equal mass. (For interpretation of the references to color in this figure legend, the reader is referred to the web version of this article.)

this ratio directly, independent of any assumption regarding the particle size distribution. A similar pair of scattering angles (at the same wavelength, λ = 265 nm) was first used by Thomas and McKay (1985) in their analysis of data from the Solar Mesospheric Explorer satellite. They showed, from data taken at pairs of complementary scattering angles, that the size range of PMC ice particles extends from mean sizes of 30 nm to above 100 nm, with the average near 70 nm (for a discussion of possible size distributions consistent with data from both CIPS and the AIM Solar Occultation for Ice Experiment, SOFIE instrument, see Bailey et al., 2015). Thus, for a specific value of FBR, it is possible to choose a corresponding mean particle size, as illustrated by the various curves in Fig. 1. When we report mode particle sizes, r_m, we use the 'standard' CIPS product (Lumpe et al., 2013), corresponding to the black curve in Fig. 1. The reader is free to choose other distributions, and hence mean particle sizes. However, it is clear that when FBR exceeds 25, the mean particle sizes will be large (relative to a typical size), regardless of the assumed distribution and particle shape.

Extracting the mean particle size begins with the removal of the Rayleigh scattering background, which is determined from nearby 'clear-sky' pixels (Lumpe et al., 2013). If a cloud is detected, then by analysis of the resulting ice scattering phase function, the size and inferred Gaussian width are determined from the ~6–7 separate measurements of cloud albedo obtained at different scattering angles. An example of this approach is shown in Fig. 2. The green asterisks are the background Rayleigh albedo, the red crosses are the resulting cloud scattering albedo after subtracting this background. A final correction is applied to normalize out the path length due to the off-nadir viewing angle, assuming horizontal orientation of the cloud layer. This yields the residual ice scattering phase function, represented by the blue diamonds. The black curve is the resulting fit (minimum χ^2) of the theoretical scattering phase function to this measured phase function. The retrieved size for this measurement set is 79 nm, which represents a weighted average over a vertical column. As discussed in Lumpe et al. (2013), the large particles (r_m > 60 nm) have large forward-scattering cross sections and thus are easily measured at these angles by the CIPS instrument even though the 90° (nadir) albedo may be very close to the detection threshold. It is important to

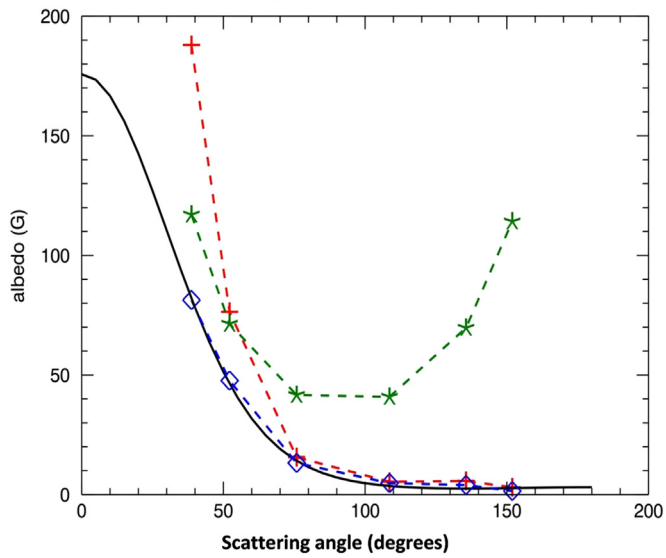

Fig. 2. An example of a CIPS particle size retrieval. Albedo (G) vs scattering angle (deg). The red line and pluses are the resulting particle scattering albedo after the removal of the Rayleigh scattering (green line). The (blue) diamonds represent the scattering function of the cloud after the scattering measurements are corrected for observation angle. The solid black line results from fitting the blue diamonds to the adopted scattering phase function. In this case the resulting mean particle size is 79 nm. (For interpretation of the references to color in this figure legend, the reader is referred to the web version of this article.)

note that the mean particle size varies with height (Romick et al., 2002; von Savigny et al., 2005; Hervig et al., 2009). We will return to the issue of the variation of particle size with height, as key to understanding the properties of a VLP-LI cloud.

Recently the Gaussian assumption has been questioned in favor of a log-normal distribution (Bailey et al., 2015). If this is a better description of reality, then the particle size values will differ. However, the numerical values of particle size are less important than the concept underlying the basic optical physics relating size to the forward scattering/backward scattering ratio. In the size range where ($2^*\pi r_m/\lambda < 3$), our T-matrix scattering results for non-spherical particles (provided by G. Baumgarten, private communication and based on the formulation by Mishchenko et al. (2000)) show that the forward-scattering asymmetry is a monotonically-increasing function of particle size. Fig. 1 shows examples of this relationship for non-spherical particle shapes. As shown in this figure for curves 2 and 3 near 80–100 nm, the 'Mie' resonance (the 'wiggles' in the two spherical-particle cases) occurs with perfect spheres (Rapp et al., 2007), but is absent in scattering by non-spherical particles.

The CIPS experiment is unique in being the first satellite experiment to observe horizontal variability in PMC brightness down to a (linear) spatial resolution of 5 km. What is surprising about these observations is that they often reveal spatially distinct regions with very large particles (60–100 nm). We arbitrarily define this VLP-LI population, as having $r_m > 60$ nm, albedo (90°) < 10 G ($1\ G = 1 \times 10^{-6}\ sr^{-1}$) and IWC $< 50\ g/km^2$. To our knowledge these events have not been observed, or at least reported, by any other observation technique.

3. Results

In Fig. 3, the measured albedo for AIM orbit 28550 (July 21, 2012) is displayed. Unless otherwise noted, albedo refers to the value at scattering angle 90°, which is the quantity reported in the CIPS Level 2 data files. The highly structured region enclosed in the box in Fig. 3 is displayed in Fig. 4. To illustrate the results for retrievals of mean ice particle size, we present images from three AIM orbits of high-spatial resolution data in Figs. 4, 7 and 8 which depict both albedo and cloud particle size. These orbits were chosen to illustrate different morphologies of the VLP-LI regions. Light-gray regions denote high albedo and dark-gray regions low albedo. Note the areas containing sizes greater than 60 nm, and the wavelike structure defined by the regions of larger size values.

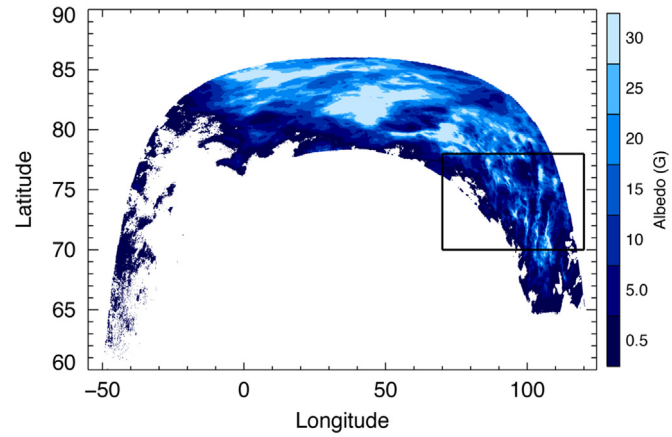

Fig. 3. CIPS measured albedo for orbit 28550. The inserted rectangle indicates the region displayed in.

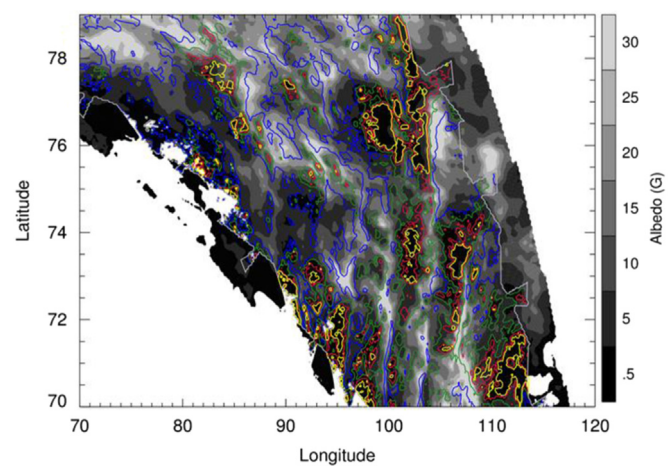

Fig. 4. A section of AIM orbit 28550 showing the measured albedo (gray scale) and contours of particle size (blue 55 nm, green 70 nm, red 85 nm, and yellow 90 nm). White areas are regions where no clouds were detected. (For interpretation of the references to color in this figure legend, the reader is referred to the web version of this article.)

For AIM orbit 28550 (Fig. 4) the regions of very large sizes lie almost always in regions of low albedo (and thus low IWC). The data show a spatially variable cloud albedo ranging from zero (the white areas where no cloud is detected) to greater than 30 G. The colored contours indicate particle sizes from 55 nm to 90 nm. The (white) areas of albedo lower than the threshold ('voids') are described in Thurairajah et al. (2013). These regions are frequently surrounded by narrow 'rims' or 'walls' of large particles. This coincidence also happens in low-albedo areas and extends down to the smallest areas observed by CIPS. Note in Fig. 4, VLP-LI (shown as the green, yellow and red contour lines) lie along a linear feature, near longitude 100° extending over the complete latitude range (70–79°) of the CIPS image. A second, less well-defined linear feature is also present. This is suggestive of a gravity wave influence, with a horizontal wavelength ~100 km. To emphasize the anti-correlation between ice particle size and albedo, Fig. 5

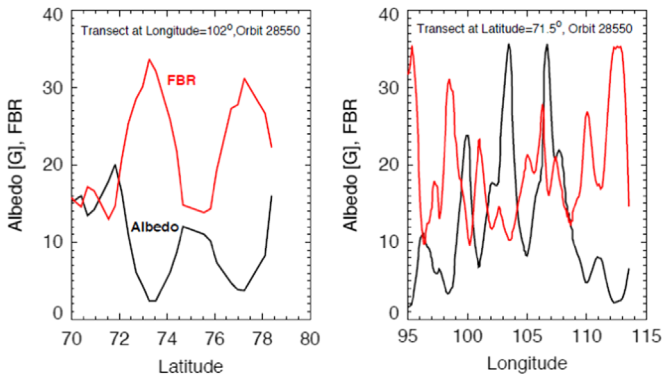

Fig. 5. Left panel: Transect of CIPS PMC image for Orbit 28550, at constant longitude. Shown are the forward/backward ratio (FBR) and the PMC albedo, smoothed by 3 pixels. The correlation coefficient is CC= −0.486 (36 points). Right panel: The same but for a transect at constant latitude, smoothed by 5 pixels. CC= −0.245 (209 points). Both correlations have significance >99%.

shows two transects for this orbit, one at constant longitude, and a second at constant latitude, with FBR and albedo plotted along each transect. This plot shows strong and statistically significant anti-correlation of albedo and FBR (and hence cloud particle size, see Fig. 1).

The distribution of CIPS measurements for orbit 28550 as a function of size is displayed in Fig. 6. This figure shows a maximum occurrence at about 45 nm, which is typical of the CIPS data set. The fall-off of particle sizes below 45 nm is due to the decreasing efficiency with decreasing particle size (Lumpe et al., 2013), and is not important in the present context. The blue curve is a Gaussian fit to the data. There is no fundamental justification for assuming a Gaussian distribution. It is adopted merely for convenience of illustration. For radii greater than about 65 nm, the data rise significantly above the Gaussian suggesting the existence of a second distinct size population. This could imply a different physical mechanism, discussed further in Section 4. Similar results (not shown) occur for the other orbits discussed below.

The dominant source of error in the retrieval of particle sizes from CIPS phase functions is the Rayleigh background subtraction. If too much (or too little) background is subtracted, the residual FBR will increase (decrease) and the particle size retrieval will be too high (or too low) (Carstens et al., 2013). Further, the change is such that the model phase function of the erroneous best fit

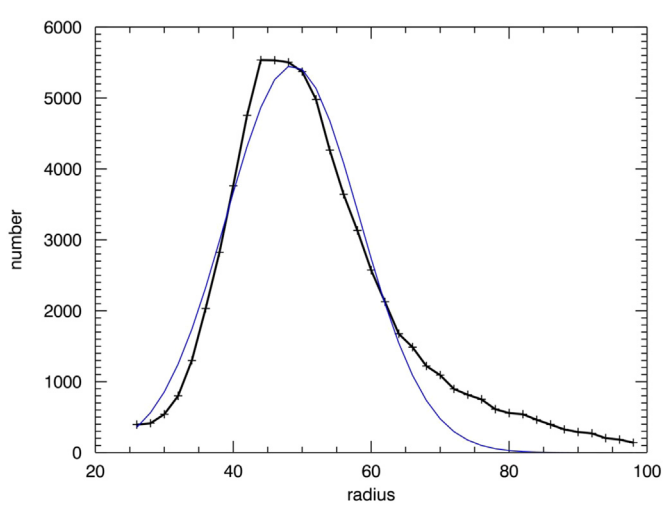

Fig. 6. The distribution of particle sizes for orbit 28550 (black crosses). The blue (solid) curve is a Gaussian fit to all the data for this orbit. Note the large particle 'tail' rising above the fit for radii >65 nm. (For interpretation of the references to color in this figure legend, the reader is referred to the web version of this article.)

particle size will continue to fit the cloud residuals very well. For a given error in the background subtraction, low-albedo clouds will have their FBR (and thus particle size) perturbed more than higher-albedo clouds. Also, since the amplitude of the background is determined at much lower spatial resolution than the cloud properties, larger areas will have very similar correlated-errors in the background subtraction. This opens the possibility that, for sufficiently dim clouds or large errors in the background, a region of low-albedo clouds can be falsely determined to have very large particles.

Fortunately, for the examples discussed in this work, this source of error is not likely to be large enough to create a VLP-LI false positive. The error decreases from low to high solar zenith angles (Lumpe et al., 2013), reducing to zero beyond ~92°. This happens because the Rayleigh background amplitude, and the sampling of the phase function improves (smaller scattering angles) with increasing solar zenith angle. Typical errors in the background amplitude are less than ~1% during the PMC season. For the example plotted in Fig. 4 (orbit 28550), a 1% reduction in the background amplitude results in a particle size error which increases from approximately −3 nm for the brighter 10 G VLP-LI clouds in the region up to −10 nm for the dimmer 2 G VLP-LI clouds. The potentially systematic error in the retrieved particle size is not large enough to change the conclusion of VLP-LI detections.

Fig. 7 shows data from a second orbit (11988, July 7, 2009) that indicates the influence of a different dynamical process. The large number of spatially close, irregularly-shaped structures of approximately 10–200 km in size, are filled with dim clouds, usually less than 5 Gs, in the center and are surrounded by low-albedo regions with large particles, reaching values up to 100 nm. Unlike orbit 28550, the structures associated with the three regions do not exhibit obvious wave-like features.

Data from a third CIPS orbit (36326, Dec. 23, 2013) from the Southern Hemisphere is shown in Fig. 8. This orbit also exhibits wave-like structures. These features extend across the entire CIPS image and, in the regions of large size and low albedo, show areas of high complexity. The image also contains voids resembling those in orbit 6607, again surrounded by 'walls' of very large particles. Imposed on the large-scale wave structures are smaller features that reveal the influence of small-scale dynamical influences. We have visually inspected hundreds of images, and when VLP-LI's exist, as they often do, they display the same general characteristics as described above.

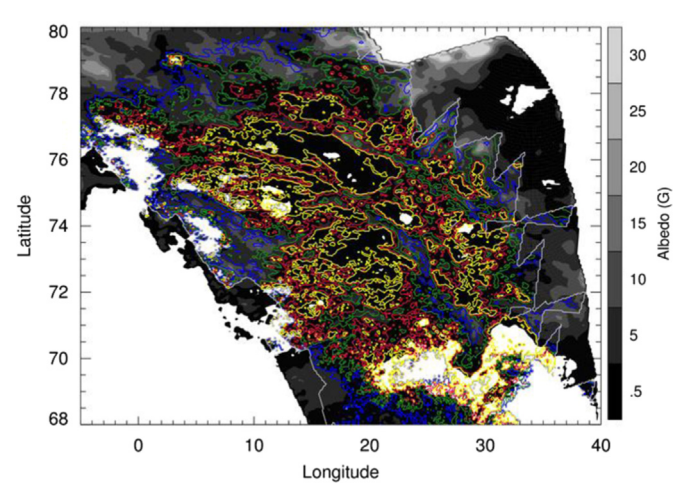

Fig. 7. Same as Fig. 4 except for AIM orbit 11988.

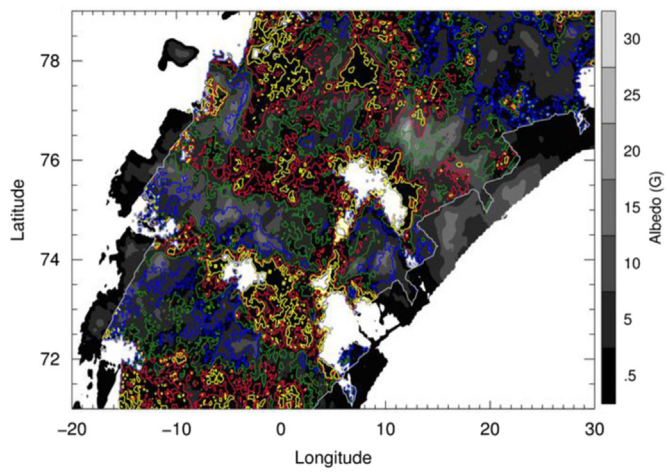

Fig. 8. Same as Fig. 4 except for AIM orbit 36325.

4. Comparison with other PMC experiments

Hultgren and Gumbel (2014) have reported isolated pockets of large particles utilizing tomographic inversion techniques using Odin/OSIRIS limb-sounding spectral data. Their technique utilizes the color-ratio method of inferring particle sizes. Using a special observing mode, they were able to perform a tomographic analysis of the altitude distribution of mode radius, along with ice number density. Their spatial resolution was ~200 km. They consistently found large particles occurring at the lowest altitudes, accompanied by low values of ice number density, consistent with the standard model and SOFIE. They generally found more numerous, moderate-sized particles at greater heights. As they point out, the contribution of this population to a (column-integrated) albedo would normally obscure the presence of the biggest particles.

5. Discussion and model results

We ask: how realistic is the assumed Gaussian distribution for the large mean particle size, e.g. $r_m = 95$ nm (Fig. 9) which extends to $r = 150$ nm in the "wings"? We need not consider particle lifetimes to answer this question – we find from a simple calculation with truncated Gaussians that if the largest particles were to disappear, either by sedimentation or sublimation at the cloud base, that the FBR would actually *decrease*. This is because the smaller particles (contributing a smaller FBR) have a greater weight when the larger particles are depleted. The observed upper limits to FBR is about 30, in agreement with calculations using the full Gaussian distribution (see Fig. 1). This means that the actual distribution must contain most particle sizes near the mean, which is the basic property of the Gaussian.

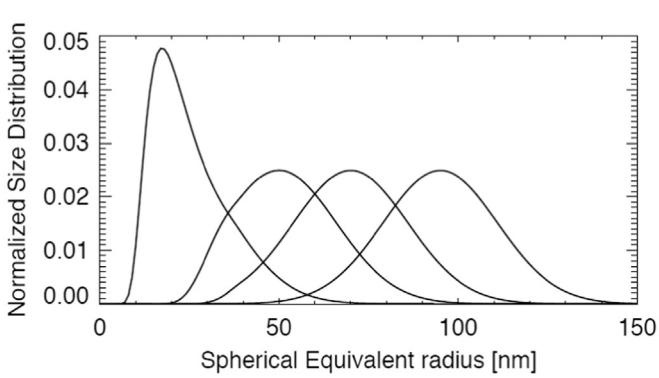

Fig. 9. Model Gaussian size distributions for four different mode radii r_m, assuming the CIPS relationship of s with r_m where s = Gaussian width. From left to right, the values of r_m are 20, 50, 70 and 95 nm. We identify the largest mode radius as representative of the "Very-Large-Particle-Low Ice" (VLP-LI) population.

We find that the spatial patterns of VLP-LI do not persist from orbit to orbit, an interval of 90 min. Assuming an ice particle begins its life from a nucleation event, the required growth rate is 60 nm/hr, a value that far exceeds 'normal' growth rates (see Fig. 11 from Lübken and Berger, 2011). It is clear that sizes > 60 nm must originate from smaller pre-existing particles. A large growth rate (up to 10 nm/hr) can be achieved from a gravity wave perturbation (see Fig. 4(d) of Chandran et al. (2012)). This process is described in detail in their paper. This requirement, together with the CIPS images which link the large-particle regions to dynamical structures (often wave-like in appearance) suggest that gravity waves may at times augment the growth process. We performed simulations from the 2D model of Chandran et al. (2012) to see if such conditions might occur with 'standard' microphysics.

5.1. Gravity wave model

The Community Aerosol and Radiation Model for Atmospheres (CARMA) model simulations of Chandran et al. (2012) show realistic variations of PMC properties in the presence of gravity waves of various wave periods and amplitudes. Linear perturbation theory is assumed. This model was shown to be in agreement with previously published 2D simulations (Jensen and Thomas, 1994; Rapp et al., 2002). For more details, see Chandran et al. (2012).

Fig. 10(a) shows model results for mean particle size from an idealized GW with a period of 5 hours, 300 km horizontal wavelength, and 6 km vertical wavelength. Fig. 3 in Chandran et al. (2012) shows the growth of PMC in the presence of this GW. For this study, we have used the same simulation. The background temperature used for this simulation are SABER temperatures at 75° N averaged for 20 days after solstice (day of year 172–192) observed during the 2008 PMC season. The water vapor profiles were obtained from observations from the Microwave Limb Sounder (MLS) instrument onboard the NASA Aura satellite for the same period during the 2008 NH PMC season. The background vertical wind profile used has been adopted from model simulations with the COMMA/IAP model (Berger and von Zahn, 1999) and was previously used in the Rapp and Thomas (2006) CARMA study. We refer the reader to Chandran et al. (2012) for a description of the treatment of horizontal and vertical winds from the GW and GW amplitude growth in the model. The cloud albedo is over-plotted as contour lines averaged for all altitudes with time on the y-axis and the horizontal domain of the model on the x-axis. It can be seen that at 22 h, the largest particle sizes correspond to the lowest-albedo clouds. Fig. 10(b) shows the anti-correlated nature of particle sizes (in red) and PMC albedo (black) at the time step of 22 h in the model simulation. The results (see Fig. 10) indicate that at a certain phase of the wave (when the cold phase of the wave coincides with the lower altitude regions between 81–84 km), particle growth is accelerated in the cold troughs of gravity waves. At this stage the water is enhanced by upward 'pumping' of enriched water vapor below the cloud base – the hydrated layer resulting from a previous sublimation event. At the same time, the warmer phase above (84–87 km) tends to destroy the ice particles. The net result is a thin layer of large particles, which does not have the usual 'overburden' of smaller, more numerous particles. In this scenario, only these large particles contribute to a column-averaged albedo, producing a VLP-LI event. Note that for this short vertical wavelength, the cold and warm regions are separated by only 3 km. It can therefore significantly modify the distribution of particles that normally fill the saturated region between 83 and 88 km (Hervig et al., 2015).

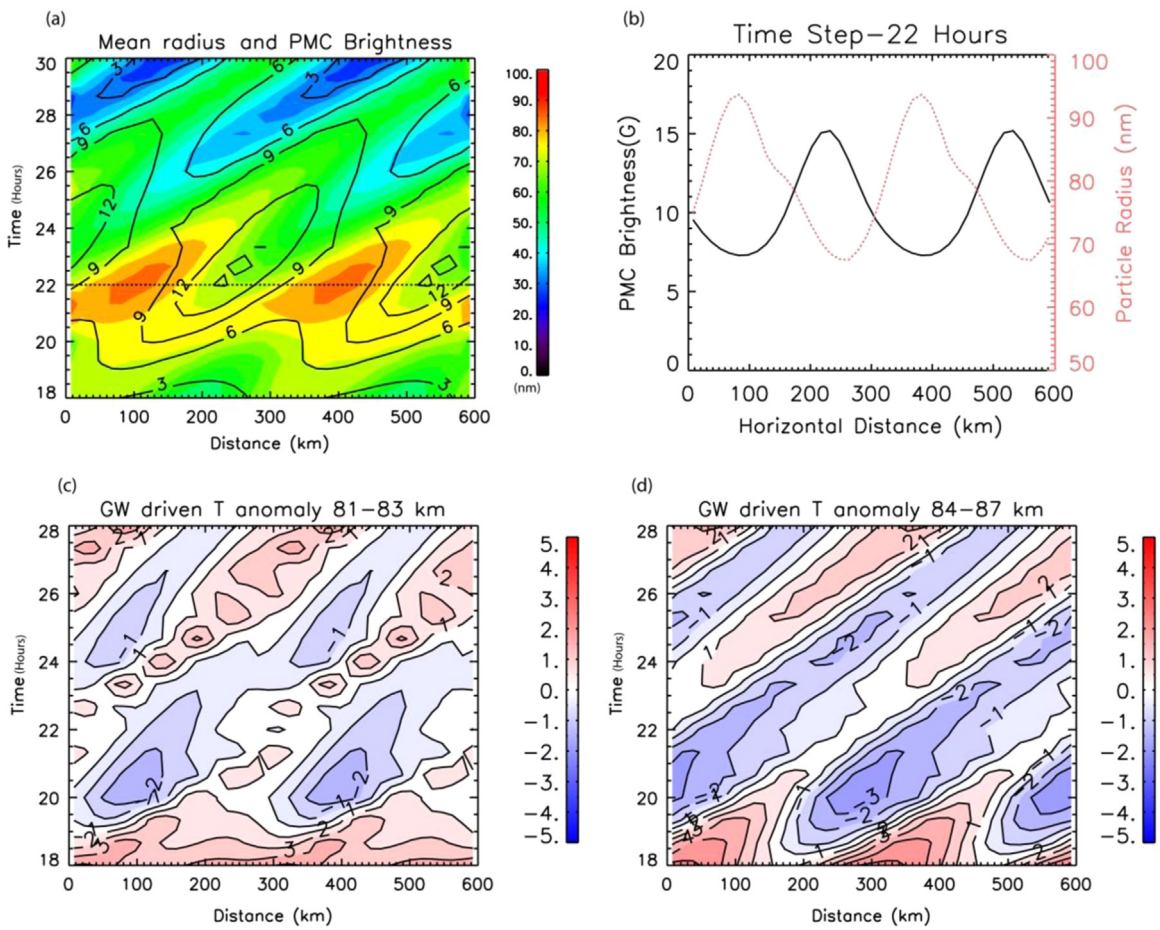

Fig. 10. (a) The PMC particle mean radius, plotted as color contours and the PMC albedo (G) over-plotted as contour lines, averaged for all altitudes. Time is shown on the *y*-axis and the horizontal domain of the model in the *x*-axis; (b) Particle sizes (in red) and PMC albedo (black) at the time step of 22 h in the model simulation; (c) Gravity wave driven temperature anomaly between 81–83 km; (d) Gravity wave driven temperature anomaly between 84–87. The modeled wave period is 5 h, and the horizontal and vertical wavelengths are 300 km and 6 km respectively. (For interpretation of the references to color in this figure legend, the reader is referred to the web version of this article.)

Figs. 10(a) and (b) are similar to the CIPS observations shown in Figs. 4, 7 and 8. Figs. 10(c) and (d) show the GW-driven temperature anomaly, calculated as variations from the background temperature at each altitude bin, between 81–83 km and 84–87 km respectively. In the lower altitude region, the cold phase of the wave corresponds to the largest particles seen in Fig. 10(a). Between 84–86 km the cold phase of the wave corresponds more to the high-albedo PMCs seen in Fig. 10(a) while the warm phase of the wave is seen in regions corresponding to the large particle size regions in Fig. 10(a), although there appears to be some time lag. Figs. 10(a) and (b) illustrate clearly that at a certain phase of the wave, the albedo and particle size are inversely related. It should be noted that the VLP-LI cloud only occurs in the first cycle of the modeled wave. Subsequent cycles do not exhibit this clear anti-correlation between albedo and size. This is gratifying because (1) the lifetime of GW packets are typically only a few cycles (Fritts and Alexander, 2003); (2) horizontal wind shears and wave-induced instabilities, and superposition of multiple gravity waves ignored in this simulation, do not have time to appreciably modify the wave. This mechanism may account for the long linear features seen in Orbit 28550 (Fig. 4).

The two-step process is illustrated by the schematic in Fig. 11, showing how the PMC particle size is modified by a short-wavelength gravity wave. In the initial state of the wave-perturbed mesopause region (a), the temperature in the upper region falls below saturation (the blue-colored area to the left of the red line illustrating the saturation border) promoting nucleation of new

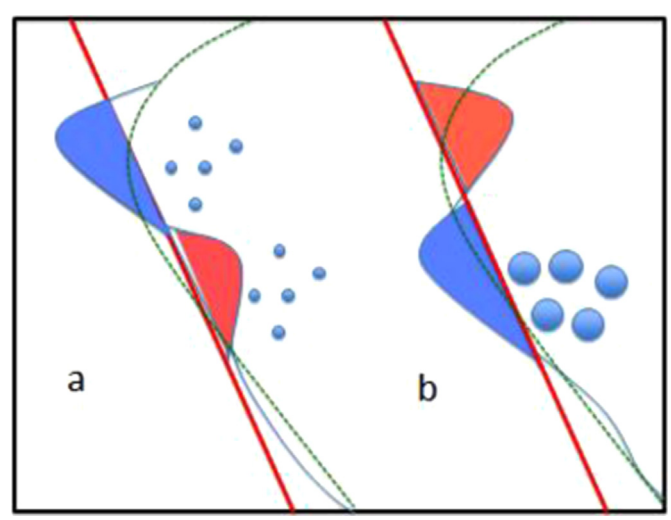

Fig. 11. Schematic showing gravity wave creation of a VLP-LI event with time (a) followed by a half-cycle later by time (b). The dashed green curve shows a normal (unperturbed) temperature profile. The curve with blue (cold) and red (warm) excursions from the normal temperature indicate a gravity wave perturbation. The red line separates the boundary between saturation (to the left) and sub-saturation to the right. The blue filled circles illustrate ice particle size. The sequence of events leading to large particles at the normal cloud base with very few particles above is described further in the text. (For interpretation of the references to color in this figure legend, the reader is referred to the web version of this article.)

particles. In the lower region, pre-existing particles may or may not survive in the sub-saturated (red) region. In the succeeding half cycle (b), the upper region is now warm and unsaturated, which prevents new particles from nucleating and is 'emptied out' due to advective descent of particles into the cold region near the "normal" cloud base. These particles grow rapidly since they are also bathed in moisture 'pumped' from the lower hydrated region. There are no overlying particles, which would otherwise dominate a nadir-pointing satellite observation – a VLP-LI.

It could be questioned whether temperature fluctuations are sufficient at all latitudes for GW's to cause the region to become sub-saturated, particularly at polar latitudes where the temperature is coldest (typically 130 K, Rong et al., 2014). It suffices to say that the CIPS images show detailed structure up to the highest latitude, including large voids. This is evidence enough that the small-scale variability in saturation conditions is sufficient to destroy ice particles at latitudes up to 85°. Thus, Fig. 11, which shows both sub- and super-saturation, appears to describe the entire summertime polar region.

5.2. WACCM/CARMA model

A similar result was produced in a 1-D CARMA simulation that used a temperature-time history from the 3-D coupled chemistry-climate Whole-Atmosphere Community Climate (WACCM) as input at each time-step into the CARMA model (Merkel et al., 2009). The temperature history was obtained by following the movement of a high latitude mesospheric air parcel over 4 days from a WACCM simulation. WACCM temperature was used to capture diverse dynamical time scales, which were indirectly simulated in CARMA by incorporating the changing temperature profile at each time-step. It is noted that small-scale gravity waves (such as the source of the previously discussed CARMA simulation) are not resolved in WACCM. This simulation, shown in Fig. 12, was part of

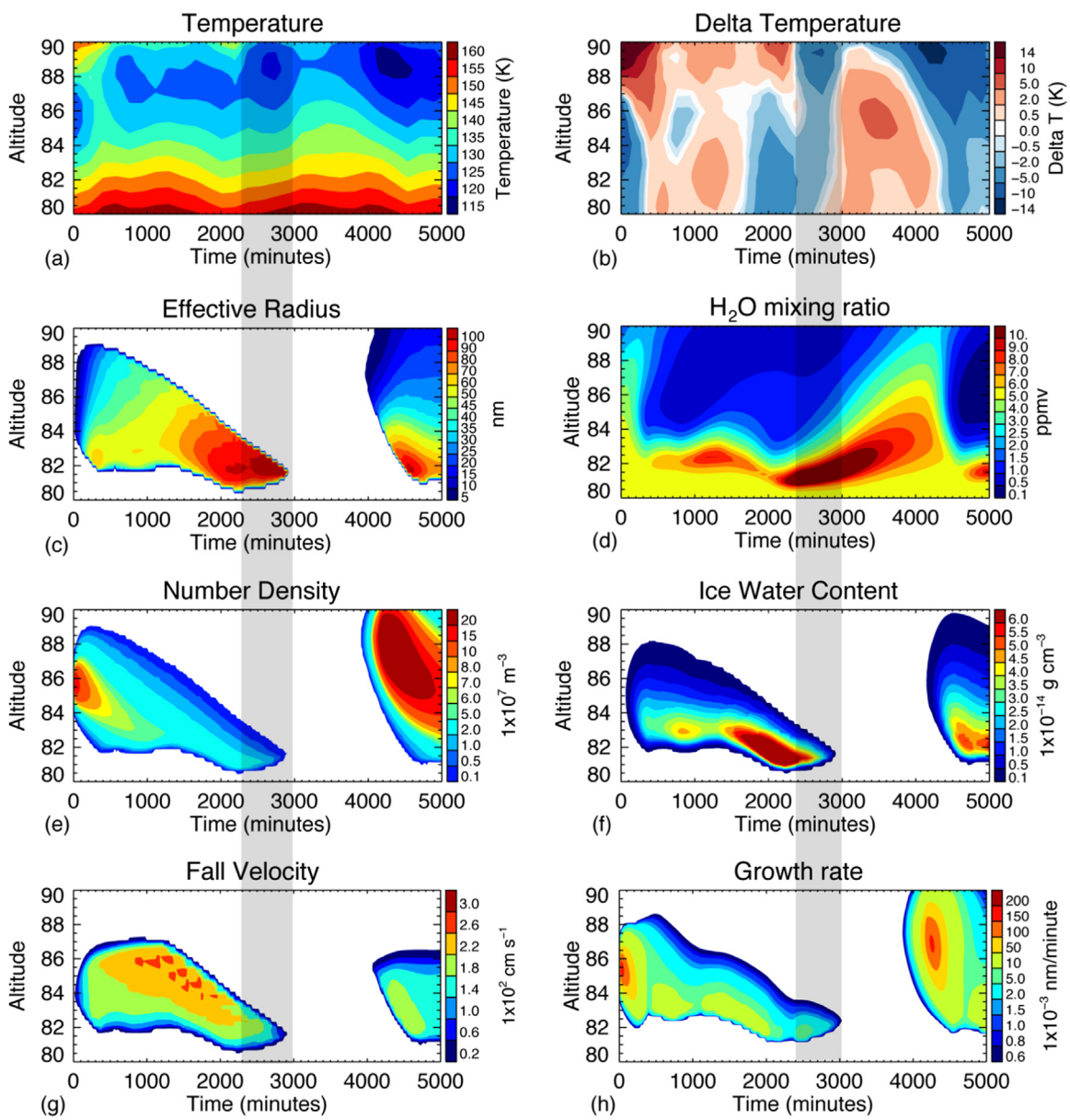

Fig. 12. Panel plots illustrating cloud properties calculated from the output of the CARMA simulation with full microphysics and particle distribution (Merkel et al., 2009). (a) Temperature time history from a WACCM simulation b) change in temperature from the mean at each altitude, (c) effective radius (area weighted), (d) water vapor mixing ratio, (e) number density, (f) ice water content (defined in Merkel et al., 2009 as ice density in g cm^{-3}), (g) mean fall velocity, and (h) growth rate. The transparent black boxes highlight the time of occurrence of a VLP-LI.

an assembly of simulations to define the relationship of effective radius (area-weighted radius), ice mass density and local temperature as discussed in Merkel et al. (2009). The panels in Fig. 12 show the evolution of PMC properties as CARMA responds to the input variables at each time step. Note that only a portion of the 4-day simulation is illustrated to highlight the occurrence of a VLP-LI. Fig. 12 shows (a) the temperature history from WACCM, (b) change in temperature from the mean at each height, (c) effective radius defined as the surface-weighted integral over the size distribution, (d) water vapor mixing ratio, (e) number density, (f) ice water content (defined in Merkel et al., 2009 as ice mass density in g-cm^{-3}), (g) mean fall speed, and (h) mean growth rate.

The simulation begins in a hydrated state with a cold mesosphere (84–88 km) that instigates nucleation followed by ice particle growth. Ice formation depletes the available water vapor and at the same time, a warming in the background temperature in the upper region ends particle creation (at about 300 min). The ambient temperature is still low enough to sustain the existing ice cloud (300–1400 min), but because of the warmer mesopause, no new particles are created at the upper heights. The existing ice particles sediment and encounter a moister environment (1500–3000 min) near 82–84 km. They continue to grow and to sediment out of the cloud until a 5 K warming trend throughout the upper mesosphere (at 3000–4000 min) sublimates the remaining ice particles. At the end of the cloud lifetime, highlighted by a transparent black box (2300–3000 min), the result is a narrow cloud region near 82 km, consisting of a small number of very large particles, with no particles above, and with low ice water content, or in short a VLP-LI cloud. Thus, the responsible processes are a cooling/nucleation, followed by an upper-altitude warming that prohibits new particle formation. The existing particles grow and sediment until there are only a few large particles left, before a warming trend causes total sublimation.

Fig. 13 shows the time varying albedo calculated for the CIPS wavelength (265 nm) for the CARMA simulation from Fig. 12. The mean radius, mean number density and mean ice water content at each time step (averaged over all altitudes) are also shown. Two regions of interest are highlighted in light blue. Between 4400–5000 min, another cloud has formed in the simulation. The cloud properties displayed represent those for a typical PMC (large number of medium-size (40 nm) ice particles with a high albedo). In contrast between 2300–3000 min, the properties of the modeled cloud are distinctly different than the typical cloud case. This shows that the simulation contains a small number of very large size (100 nm) particles with low albedo and low ice density – again a VLP-LI cloud.

The appearance of VLP-LI clouds at the perimeter of the region of cloud absence in both the CIPS images and in Fig. 13 may provide a clue regarding the nature of large semi-circular voids. If voids are caused by an occasional downward descent of a column of air which warms the region (by adiabatic compression), the cooler edge-regions would show evidence of its downward progression as a VLP-LI. The void itself may then represent the area where the downward descent of air has completely eliminated the cloud.

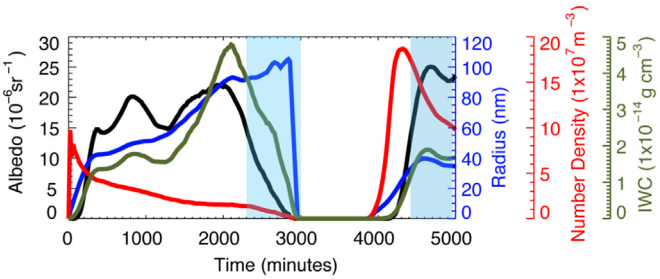

Fig. 13. Time dependent relationships between model albedo, effective radius, number density and IWC, all vertically-averaged. The shaded regions are of special interest (see text).

We find from the full AIM data set that, depending upon season and hemisphere, VLP-LI occupy 5 to 40% of the total image area. It is clear that previous satellite measurements are not sensitive to such small-scale events. The small contribution from VLP-LI to the scattered light (or to the cloud extinction in the case of AIM SOFIE) is obscured by larger contributions from the smaller, but more numerous particles. Furthermore in previous limb and large field-of-view nadir observing techniques, their association of VLP-LI with dynamical features is lost in the several-hundred km averaging process. The field of view of the SBUV (Solar Backscattered Ultraviolet experiment; see DeLand and Thomas, 2015) satellite instrument is 150 × 150 km. It is possible that the larger-scale VLP-LI could be identified in nadir hyperspectral observations by the Ozone Monitoring Instrument (OMI on the Aura satellite; see DeLand et al., 2010). The smallest OMI pixel size is 13 × 48 km at the nadir. A forthcoming Swedish satellite investigation (Mesospheric Airglow/Aerosol Tomography and Spectroscopy, or MATS) will provide horizontally- and height-resolved PMC structures which may be capable of detecting the larger VLP-LI events (Gumbel et al., 2015). The best PMC data set which could at least support the size-albedo anti-correlations is from the ALOMAR lidar (Baumgarten et al., 2002).

The most advanced general circulation models that are coupled with a microphysics module also have resolutions of many hundreds of kilometers. Although they are capable of simulating the largest voids seen by CIPS, they do not simulate the smaller structures evident in CIPS images. We hope that this work will motivate modelers to perform higher-resolution simulations that can be used to pursue analysis of their origin and associations of VLP-LI with the edges of voids.

6. Summary and conclusions

High-resolution nadir imaging data from the CIPS instrument on the AIM spacecraft have revealed detailed relationships between large PMC particles (mean radii $r_m > 60$ nm) and low UV cloud albedo (A (265 nm) $< 10 \times 10^{-6}$ sr^{-1}). These very-large-particle-low-ice events, or for short, VLP-LI regions, occur over spatial extents ranging from ~100 km down to the smallest resolution element of the CIPS cameras (25 km^2). The data indicate the existence of specific dynamical processes not generally captured by models with comparatively large resolution. PMC are usually observed at the earth's limb or in the nadir with large fields of view. Because of their inherent (horizontal) averaging over hundreds of kilometers, previous measurements have failed to capture the striking anti-correlation of albedo and particle size. This limitation has also prevented them from finding an association of large particles with gravity waves and cloud voids (regions in which no ice above the detection threshold are present).

Based on two different microphysical model simulations, we suggest that the responsible processes are a warming in the upper part of the saturated region of ice occurrence, combined with a cooling lower down at the normal cloud base. This causes sublimation of the smaller, but more numerous ice particles and whose scattering contributions normally 'hide' the lowermost large particles at the cloud base. We speculate that small-scale processes, such as gravity wave perturbations (with short vertical wavelengths) of the wind and temperature fields are partly responsible. The cloud voids are often seen to be surrounded by 'walls' of large ice particles (with mean sizes up to 100 nm). The mean sizes often decrease with distance away from their

perimeter. The close association of large particles with voids suggests a second mechanism – a downward-directed wind arising from above the cloud region, which progressively warms the mesopause region as it descends. This process first eliminates the more numerous top-side particles by sublimation, leaving exposed, at least temporarily, the largest particles of a previously-existing populations at the cloud base (near 81–83 km). The CIPS images portray a previously unrecognized coupling of ice microphysics with dynamics, thereby providing a new window into the small-scale (5–100 km) phenomena of the summertime mesosphere. Future work will study year to year variations in the occurrence rate of VLP-LI.

Acknowledgments

This work was supported by the NASA/AIM mission, which is funded by NASA's Small Explorers Program under contract NAS5-03132. Many thanks to the AIM team for years of dedication and service. We benefitted from discussions with D. Fritts, G. Baumgarten, H. Wilms and C. Bardeen. We thank O. Christensen for providing calculations for the sedimentation speeds of ice particles, and G. Baumgarten for providing T-matrix calculations for non-spherical particle scattering properties.

References

Bailey, S.M., Thomas, G.E., Hervig, M.E., Lumpe, J.D., Randall, C.E., Carstens, J.N., Thurairajah, B., Rusch, D.W., Russell, J.M., Gordley, L.L., 2015. Comparing nadir and limb viewing observations of polar mesospheric clouds: The effect of the assumed particle size distribution. J. Atmos. Sol. Terr. Phys. . http://dx.doi.org/10.1016/j.jastp.2015.02.007

Baumgarten, G., Fricke, K.H., von Cossart, G., 2002. Investigation of the shape of noctilucent cloud particles by polarization lidar technique. Geophys. Res. Lett. 29 (13), 1630. http://dx.doi.org/10.1029/2001GL013877.

Baumgarten, G., Fiedler, J., Lübken, F.-J., von Cossart, G., 2008. Particle properties and water content of noctilucent clouds and their interannual variation. J. Geophys. Res. 113, D06203. http://dx.doi.org/10.1029/2007JD008884.

Berger, U., von Zahn, U., 1999. The two-level structure of the mesopause: a model study. J. Geophys. Res. 104 (D18). http://dx.doi.org/10.1029/1999JD900389.

Berger, U., von Zahn, U., 2002. Icy particles in the summer mesopause region: three-dimensional modeling of their environment and two- dimensional modeling of their transport. J. Geophys. Res. 107 (A11), 1366. http://dx.doi.org/10.1029/2001JA000316.

Chandran, A., et al., 2012. Atmospheric gravity wave effects on polar mesospheric clouds: a comparison of numerical simulations from CARMA 2D with AIM observations. J. Geophys. Res., 117.

DeLand, M., Thomas, G., 2015. Updated PMC trends derived from SBUV data. J. Geophys. Res., 120. http://dx.doi.org/10.1002/2014JD022253.

DeLand, M., Shettle, E., Thomas, G., Olivero, J., 2010. Direct observations of PMC local time variations by Aura OMI. J. Atmos. Sol. Terr. Phys. 73, 2049–2064. http://dx.doi.org/10.1016/j.jastp.2010.11.019.

Fritts, D., Alexander, J., 2003. Gravity wave dynamics and effects in the middle atmosphere. Rev. Geophys. 41. http://dx.doi.org/10.1029/2001RG000106.

Fritts, D., Isler, J., Thomas, G., 1993. Wave breaking signatures in noctilucent clouds. Geophys. Res. Lett. 20, 2039–2042.

Gumbel, J., et al., 2015. The MATS satellite mission-tomographic perspectives on the mesosphere. Presentation at the International Workshop on Layered Phenomena in the Mesopause Region, July, 2015, Boulder, CO.

Hervig, et al., 2009. SOFIE PMC observations during the northern summer of 2007. J. Atmos. Sol. Terr. Phys. 71, 331–339.

Hervig, M., Siskind, D., Bailey, S., Russell III, J., 2015. The influence of PMCs on water vapor and drivers behind PMC variability from SOFIE observations. J. Atmos. Sol. Terr. Phys. 132, 124–134.

Hultgren, K., et al., 2013. First simultaneous retrievals of horizontal and vertical structures of Polar Mesospheric Clouds from Odin/OSIRIS. J. Atmos. Sol. Terr. Phys. . http://dx.doi.org/10.1016/j.jastp.2013.06.013

Hultgren, K., Gumbel, J., 2014. Tomographic and spectral views on the life cycle of polar mesospheric clouds from Odin/OSIRIS. J. Geophys. Res. Atmos. 119. http://dx.doi.org/10.1002/ 2014JD022435.

Hultgren, K., Gumbel, J., 2014. Tomographic and spectral views on the lifecycle of polar mesospheric clouds from Odin/OSIRIS. J. Geophys. Res.

Jensen, E., Thomas, G., 1994. Numerical simulations of the effects of gravity waves on noctilucent clouds. J. Geophys. Res. 99, 3421–3430.

Lumpe, J., et al., 2013. Retrieval of polar mesospheric cloud properties from CIPS: algorithm description, error analysis and cloud detection sensitivity. J. Atmos. Sol. Terr. Phys. 104, 167–196. http://dx.doi.org/10.1016/j.jastp.2013.06.007.

McClintock, et al., 2009. The cloud imaging and particle size experiment on the aeronomy of ice in the mesosphere mission: Instrument concept, design, calibration and on-orbit performance. J. Atmos. Sol. Terr. Phys. 71 (3–4), 340–355. http://dx.doi.org/10.1016/j.jastp.2008.10.011.

Merkel, A., et al., 2008. Mesospheric planetary wave effects on global PMC variability inferred from AIM–CIPS and TIMED–SABER for the northern summer 2008 PMC season. J. Atmos. Sol. Terr. Phys. 71 (3–4), 381–391. http://dx.doi.org/10.1016/j.jastp.2008.12.001.

Merkel, A., Marsh, D., Gettelman, A., Jensen, E., 2009. On the relationship of polar mesospheric cloud ice water content, particle radius and mesospheric temperature and its use in multi-dimensional models. Atmos. Chem. Phys. 9, 8889–8901. http://dx.doi.org/10.5194/acp-9-8889-2009.

Mishchenko, M.I., Hovenier, J.W., Travis, L.D., 2000. Light Scattering by Nonspherical Particles. Elsevier, New York.

Rapp, M., et al., 2002. Small-scale temperature variations in the vicinity of NLC: experimental and model results. J. Geophys. Res. 107, 4392. http://dx.doi.org/10.1029/2001JD001241.

Rapp, M., Thomas, G., 2006. Modeling the microphysics of mesospheric ice particles: assessment of current capabilities and basic sensitivities. J. Atmos. Sol. Terr. Phys. 68, 715–744.

Rapp, M., Thomas, G., Baumgarten, G., 2007. Spectral properties of mesospheric ice clouds; evidence for nonspherical particles. J. Geophys. Res. 112, D03211. http://dx.doi.org/10.1029/2006JD007322.

Romick, G., Carbary, J., Morrison, D., 2002. Satellite observations of the spectra of polar mesospheric clouds at different altitudes. Br. Astron. Assoc. Memo. 45, 172, London.

Rong, P.P., Russell III, J.M., Randall, C.E., Bailey, S.M., Lambert, A., 2014. Northern PMC brightness zonal variability and its correlation with temperature and water vapor. J. Geophys. Res. Atmos. 119, 2390–2408. http://dx.doi.org/10.1002/2013JD02051.

Rusch, D., et al., 2009. The cloud imaging and particle size experiment on the Aeronomy of Ice in the Mesosphere mission: cloud morphology for the northern 2007 season. J. Atmos. Sol. Terr. Phys. 71, 356–364. http://dx.doi.org/10.1016/j.jastp.2008.11.005.

Russell III, J.M., et al., 2009. Aeronomy of Ice in the Mesosphere (AIM): overview and early science results. J. Atmos. Terr. Phys. 71 (3–4), 289–299. http://dx.doi.org/10.1016/j.jastp.2008.08.011.

Thomas, G.E., McKay, C.P., 1985. On the mean particle size and water content of polarmesospheric clouds. Planet. Space Sci. 33 (10), 1209–1224.

Thurairajah, B., et al., 2013. Morphology of polar mesospheric clouds as seen from space. J. Atmos. Sol. Terr. Phys. 104, 234–243.

von Savigny, C., 2005. Vertical variation of NLC particle sizes retrieved from Odin/OSIRIS limb scattering observations. Geophys. Res. Lett. . http://dx.doi.org/10.1029/2004GL021982

Witt, G., 1962. Height, structure and displacement of noctilucent clouds. Tellus XIV.